Lawrence Berkeley National Laboratory

Title

Revisiting the role of Zr doping in Ni-rich layered cathodes for lithium-ion batteries

Permalink

https://escholarship.org/uc/item/5kv3c5h6

Journal

Journal of Materials Chemistry A, 9(32)

ISSN

2050-7488

Authors

Jung, Chul-Ho
Li, Qingtian
Kim, Do-Hoon
et al.

Publication Date

2021-08-17

DOI

10.1039/d1ta04450h

Peer reviewed

Revisiting the role of Zr doping in Ni-rich layered cathode for lithium-ion batteries

Chul-Ho Jung[a], Qingtian Li[b], Do-Hoon Kim[a], Donggun Eum[a], Donghyun Ko[c], Jonghyun Choi[a], Jongwon Lee[a], Kyeong-Ho Kim[a], Kisuk Kang[a], Wanli Yang[b] and Seong-Hyeon Hong*[a]

The realization of high performance Ni-rich layered cathodes remains a challenge because of the multiple degradation factors that concurrently operate during battery cycling. In particular, depletion of oxygen charge and consequent lattice-oxygen instability at deep charge state accelerate the subsequent chemomechanical degradation mechanisms. Among the proposed methodologies, doping has proven to be effective in enhancing the cathode cycle life by stabilizing the layered structure. Herein, we achieved the electrochemically stabilized Ni-rich $LiNi_{0.92}Co_{0.04}Mn_{0.04}O_2$ through Zr doping, resulting in a 15% increase of the capacity retention after 100 cycles. In-depth investigations are conducted to unveil the effects of Zr doping on the layered cathode, and in particular, the critical role of Zr doping on the lattice oxygen stability is systematically studied. By combining state-of-the-art magnetometer characterization, X-ray analysis, and first-principles calculation, we reveal that Zr doping positively contributes the to lattice oxygen stability by alleviating the oxygen charge loss at deep charge , thereby improving the cathode electrochemical reversibility. Our findings provide an insight into the Zr doping mechanism and help to design the Ni-rich layered oxides for future applications.

.

1 Introduction

With the advent of electrical vehicles (EVs), there is a pressing demand to develop the lithium ion battery (LIB) cathode materials with a high specific energy at a reduced cost.[1,2] In this sense, three-component $LiNi_xCo_yMn_{1-x-y}O_2$ (LNCM), which has the same crystal structure as the state-of-the-art $LiCoO_2$ layered oxide, has solidified its status as a cathode material of choice for EV battery systems.[3,4] To further boost the practical capacity of LNCM, research efforts are now focused on developing the LNCM materials with a high Ni content (x ≥ 0.9), that is, Ni-rich layered oxides.[5]

Nevertheless, the practical implementation of Ni-rich layered

[a] Department of Materials Science and Engineering and Research Institute of Advanced Materials, Seoul National University, Seoul 08826, Republic of Korea. E-mail: shhong@snu.ac.kr
[b] Advanced Light Source, Lawrence Berkeley National Laboratory, Berkeley, California 94720, USA
[c] Department of Electrical and Computer Engineering, Inter-University Semiconductor Research Center, Seoul National University, Seoul 08826, Republic of Korea

oxides is currently hindered by their continuous capacity fading and especially, the deterioration becomes increasingly severe with the increase of Ni content or at a high state of charge (SOC).[6-8] Extensive researches have been performed to unveil the Ni-rich LNCM degradation mechanisms, which are reported to be abrupt anisotropic lattice contraction upon deep charge,[9] structure and chemical instability,[10,11] and electrolyte decomposition.[12] All of the above mechanisms concurrently operate from the particle surface to the bulk and jeopardize the successful application of Ni-rich LNCM.

As the mechanistic link between these failure mechanisms remains ambiguous, they have been perceived as independent phenomena; however, many reports have proposed and provided the evidence of the correlation between each mechanism when viewed on the atomic scale.[13,14] In particular, the instability of lattice oxygen upon deep charge is being considered as one of the critical origins of the general capacity fading mechanisms in layered oxides.[15-17] From the perspective of the crystal/electronic structure of layered oxides, cubic-closed-packed (ccp) oxygen layers serve as the backbone of the layered crystal structure while the Li and transition metal (TM) occupy the interstitial sites along the $[111]_{cubic}$ direction ($[001]_{hexagonal}$ direction).[18] In this way, the 2p orbital of the oxygen ligand hybridizes with the TM 3d orbitals along the linear Li–O–TM configuration under octahedral symmetry.[19] By virtue of the TM(3d)–O(2p) hybridization, d holes generated on O 2p orbitals upon high SOC lead to the depletion of oxygen charge density and resultant oxygen instability,[20-23] which accelerates the oxygen gas release,[24] electrolyte oxidation,[12,25] surface-reconstructed-layer (SRL) formation,[26,27] sudden lattice contraction,[28] and mechanical damage.[14,29] In this sense, it can be postulated that the stabilization of the lattice oxygen upon deep charge might be critical to improve the cycle life of Ni-rich layered cathodes.

Numerous strategies have been considered to promote the layered cathode cycle life including foreign doping,[30] surface treatment,[31] microstructure control,[32] and compositional gradients.[33] Among the proposed strategies, the lattice doping is one of the most prevailing and suitable methodologies to address the aforementioned issues of Ni-rich LNCM. Despite some

controversy surrounding the doping mechanisms, various dopants from low-valent Mg^{2+} to high-valent W^{6+} have been investigated for the layered cathodes.[34,35] In particular, Zr doping has been widely adopted for the layered oxides with various Ni contents, which is attributed to its effectiveness in improving the battery performance and its low cost.[34, 36-40] Even though the previous studies have verified the positive effect of Zr doping on the cathode electrochemical performance, there is still lack of understanding the beneficial effects of Zr doping mechanism on Ni-rich layered oxides. Specifically, an in-depth study of Zr doping effects on the lattice oxygen stability upon deep charge has not yet been performed, which requires further investigation of Zr doping in Ni-rich layered cathodes.

In this study, we provide the comprehensive analyses of the Zr doping effects in a $LiNi_{0.92}Co_{0.04}Mn_{0.04}O_2$ LIB cathode material with a focus on unveiling the origin of its mechanism. First, by combining spectroscopy and microscopy techniques, we show that Zr doping enhances the electrochemical performance of LNCM by affecting the abrupt c-axis contraction, particle cracks, oxygen evolution, electrolyte decomposition, and Li–Ni disorder, thus alleviating the diverse LNCM degradation factors. Then, the role of Zr doping on the oxgen stability is systematically investigated with the aid of state-of-the-art Squid-VSM, resonant inelastic X-ray scattering (RIXS), and scanning transmission X-ray microscopy (STXM) analyses. According to the measurements, it is revealed that Zr doping suppresses the oxygen oxidation upon high SOC, which is associated with the oxygen instability and aforementioned degradation factors. These experimental findings are further collaborated by first-principles calculations showing that the Zr doping was effective in alleviating the oxygen charge depletion upon high SOC.

2 Experimental

2.1. Materials Preparation. $Ni_{0.92}Co_{0.04}Mn_{0.04}(OH)_2$ hydroxide was synthesized by a co-precipitation method using $NiSO_4 \cdot 6H_2O$ (Daejung Chemical Co.), $CoSO_4 \cdot 7H_2O$ (Daejung Chemical Co.), $MnSO_4 \cdot H_2O$ (Daejung Chemical Co.), NaOH (Daejung Chemical Co.), and NH_4OH (Daejung Chemical Co.). The mixed solution (Ni: Co: Mn= 92: 4: 4 in molar ratio) was pumped into the reactor containing a solution of NaOH (aq) and NH_4OH (aq) under N_2 atmosphere. Simultaneously, NaOH (molar ratio of NaOH/TM=2.0) and NH_4OH (molar ratio of NH_4OH/TM=1.2) were separately fed into the reactor. Afterwards, the hydroxide precursor was obtained by filtering, washing, and vacuum drying the precipitate for overnight. To prepare the undoped LNCM (U-LNCM), the hydroxide precursor was mixed with $LiOH \cdot H_2O$ (precursor: Li=1: 1.03 in molar ratio) and calcined at 740 °C for 12 h under an oxygen flow. For the synthesis of Zr-doped LNCM (Zr-LNCM), the hydroxide precursor was first coated with Zr source using zirconium butoxide solution (Sigma-Aldrich) and acetylacetone (Sigma-Aldrich). In detail, zirconium butoxide solution and acetylacetone (1: 4 in mole ratio) was first homogenously mixed in dehydrated ethanol for 30 min. Then, the hydroxide precursor (Zr: NCM=1: 99 in mole ratio) was added into the solution, stirred for 30 min, filtered, and then, dried under 100

°C overnight. Finally, to obtain the Zr-LNCM, the dried powder was mixed $LiOH \cdot H_2O$ with a molar ratio of 1: 1.03 and calcined at the same conditions with the U-LNCM.

2.2. Characterization. The chemical composition of the prepared LNCM was determined by inductively coupled plasma-atomic emission spectroscopy (ICP-AES) (OPTIMA 4300DV, PerkinElmer). The crystal structure and lattice parameters were determined by synchrotron radiation powder X-ray diffraction (HRRD), which was collected at room temperature from the 9B HRPD beamline at the Pohang Accelerator Laboratory (PAL). Fullprof program was used for the Rietveld refinement. The in-situ battery cell X-ray diffractometer (R-AXIS IV, RIGAKU) was used to observe the phase transitions during charging with a modified coin-type cell (3 mm hole at its center sealed with mylar film). The electrodes were pre-cycled before the measurement. The in-situ XRD was conducted by charging the voltage up to 4.4 V vs Li/Li^+ with a 0.2 C current density while the diffraction patterns were recorded every 10 min. For the after cycled analyses (temperature-resolved XRD, SEM, TEM, EELS, Squid-VSM, STXM, mRIXS, and sPFY), the coin-cells were dissembled in a glove box after the cells reached the designated SOC (x=0.8, x=0.88, $Li_{1-x}NiO_2$) or after 50 cycles. Then, the dissembled electrodes were washed in DMC (dimethyl carbonate) to remove the residual lithium salt. For the temperature-resolved XRD (X'Pert PRO, KIST) measurement, the XRD patterns were collected while heating the sample from room temperature to 600 °C with a heating rate of 8 °C /min under the He carrier-gas flow. The SEM (SU-70, Hitachi) and TEM (JEM-2100F, JEOL) were used to observe the particle morphology. The high-resolution STEM images and electron energy loss spectroscopy (EELS) data were collected from the double aberration-corrected JEOL-ARM 200CF microscope with a cold-field emission gun operated at an acceleration voltage of 200 kV. The cross sectioned samples were prepared by FIB (Helios Nano Lab450, FEI) and cross-section polisher (IB-19510CP, JEOL) for TEM and SEM analyses, respectively. For Squid-VSM analysis (QM02, magnetic property measurement system), the cathode material was scratched off from the current collector and ~20 mg of powders was used for the analysis. The temperature-dependent magnetic moment was measured by varying the temperature from 5 K to 300 K. The magnetic susceptibility was calculated by dividing the magnetization by the magnetic field. To obtain the Ni L_3-edge spectra, scanning transmission X-ray microscopy (STXM) analysis was performed at beamline 10A at the PAL. For the STXM analysis, DMC washed electrodes were scarapped of the electrodes and further sonicated in DMC solvent for ~30 min. Then, the solvent was drop-cast onto carbon-coated Cu TEM grid for the STXM measurement. Mapping of resonant inelastic X-ray scattering (mRIXS) was measured in iRIXS endstation at BL8.0.1 of the Advanced Light Source at Lawrence Berkeley National Laboratory. The emission and excitation energy resolutions were about 0.3 and 0.2 eV, respectively, without considering the core-hole life time broadening. Data were collected with an excitation energy step of 0.2 eV across the whole O K-edge range. O-K mRIXS-sPFY data were collected by integrating the mRIXS intensity within the emission energy from 523 to 525 eV.

2.3. Electrochemical Measurements. The electrochemical properties were analyzed with 2032 coin-type cells (Welcos, Korea), which were fabricated in Ar-filled glove box. The positive electrodes were prepared by casting a slurry mixed with active material, Super P, and polyvinylidene fluoride (PVDF) binder (85:8:7 in weight ratio) onto an Al foil with a mass loading of ~8 mg cm^{-2}. The cell was fabricated using Li-metal as a counter electrode with a separator film (Celgard) filled with LiPF$_6$ (1.2 M) solution dissolved in an ethyl carbonate-ethyl methyl carbonate mixture (3:7 *v/v*). The half-cells were tested at voltage between 2.5 and 4.4 V vs Li/Li$^+$ at room temperature using automatic battery cycler (WBCS 3000S WonATech). The current density of 1 C represents 200 mA g^{-1}. For the galvanostatic intermittent titration technique (GITT) measurement, the half-cell was applied 0.2 C current for 10 min and subsequently rested for 1 h (voltage range 2.5~4.4 V). The EIS (ZIVE SP1 potentiostat/galvanostat/EIS) analysis were taken in a frequency range of 1000 kHz~5 mHz with an AC amplitude of 10 mV. To prepare the electrodes for the differential electrochemical mass spectrometry (DEMS) analysis, the obtained powders were prepared into the slurry and casted onto the Al mesh (AL008772, Goodfellow) with ~10 mg cm^{-2} mass loading. Then, the cathodes were fabricated in a glove box using Li metal as counter electrode. The details for DEMS experimental setup are provided elsewhere.[41] For the DEMS analysis, the cell was charged to 4.8 V with a 0.1 C current density.

2.3. First Principles Calculations (DFT). All calculations in this work were performed based on spin-polarized density functional theory (DFT) implemented in Vienna ab-initio simulation package (VASP).[42] Projector augmented wave (PAW) pseudo-potentials were used and all energies were calculated within spin-polarized generalized gradient approximation with Hubbard-U (GGA+U) parametrization using Perdew-Burke-Ernzerhof (PBE functional).[43,44] The onsite Coulomb parameter U of 6.4 eV was applied to nickel 3d electrons according to the value in the previous works.[45] A kinetic energy cutoff of the plane-wave basis set was 500 eV and a 2×2×1 k-points monkhorst-pack grids were utilized for the bulk relaxation (Li$_{12}$Ni$_{11}$Zr$_1$O$_{24}$) so that the structures were fully relaxed within the interatomic forces smaller than 0.02 eV/Å (Table S1). To describe the delithiated states (Li$_2$Ni$_{11}$Zr$_1$O$_{24}$ and Li$_4$Ni$_{11}$Zr$_1$O$_{24}$), the 30 lowest energy configurations were chosen for each delithiated state using Ewald summation.[46] All configurations were fully relaxed. Charge transfer between nickel and oxygen was quantified with bader charge analysis.[47]

3 Results

The crystal structure of as-synthesized undoped and Zr-doped LiNi$_{0.92}$Co$_{0.04}$Mn$_{0.04}$O$_2$ powders (denoted as U-LNCM and Zr-LNCM, respectively) was determined using high resolution powder diffraction (HRPD) (Fig. 1a and b). All the diffraction peaks were indexed based on the hexagonal α-NaFeO$_2$-type layer structure (space group R-3m) without a secondary phase.[35] The Rietveld refinement results indicated that the lattice parameters and unit-cell volume slightly increased with Zr doping, indicating that Zr^{4+} was successfully incorporated into the LNCM lattice (Fig. 1c, Fig. S1†, Table S2). The increase of lattice constants can be attributed to the larger ionic radius of Zr^{4+} (0.72 Å, CN (coordination number) = 6) compared with that of Ni^{2+} (0.69 Å), Co^{3+} (0.545 Å), and Mn^{4+} (0.53 Å) with CN=6.[37,48] The chemical composition of the as-synthesized powders was analyzed using inductively coupled plasma atomic emission spectroscopy (ICP-AES) (Table S3). The relative mole fraction of Ni: Co: Mn was close to the nominal composition of 92: 4: 4 in both LNCM powders, and the Zr doping concentration was estimated to be approximately 1 mol%. The SEM images of as-synthesized U-LNCM and Zr-LNCM revealed that both powders were more or less spherical with a diameter of 7–8 μm and were composed of densely packed primary particles of ~500 nm (Fig. 1d and 1e). Apparently, Zr doping had no effect on the morphology and size of the primary/secondary particles. The EDS mapping on the cross-sectioned polished particles showed that Zr was homogeneously distributed throughout the particles (Fig. 1f), indicating that Zr was uniformly incorporated into the LNCM crystal structure. The cross-section polished SEM image of pristine U-LNCM is provided on Figure 3b.

After confirming the Zr doping, as-synthesized powders were prepared into a slurry and coated on Al foil using the doctor blade method for the electrochemical testing. The electrochemical reactions of U-LNCM and Zr-LNCM electrodes were evaluated using 2032 coin-type half-cells in the potential range of 2.5–4.4 V (vs. Li/Li$^+$) (Fig. 2). The electrodes had similar initial charge/discharge voltage profiles and delivered similar initial discharge capacities (U-LNCM: 230.1 mAh g^{-1} and Zr-LNCM: 225.2 mAh g^{-1}) at a current density of 0.1 C (1 C= 200 mA g^{-1}) (Fig. 2a). The slightly lower discharge capacity of Zr-LNCM electrode was resulted from the incorporation of electrochemically inactive Zr.[39] However, the capacity retention of U-LNCM electrode was significantly improved with the introduction of Zr. After 100 cycles at a current density of 0.3 C, approximately 83% of the initial capacity was retained in the Zr-LNCM electrode, whereas the U-LNCM electrode retained only 68% of its initial capacity (Fig. 2b). When the current density was lowered to 0.1 C at the last cycle, the U-LNCM electrode delivered a capacity of 177.5 mAh g^{-1}, whereas the Zr-LNCM electrode delivered a much higher capacity of 220.4 mAh g^{-1}. In addition, 0.5, 1.5, and 2.0 mol% Zr-doped LNCM powders were prepared, and their cycle performance was investigated (Fig. S2†). After 100 cycles at 0.3 C, the reversible capacity was highest for the 1.0 mol% Zr-doped LNCM electrode, and thus, the subsequent analysis was conducted on this electrode. To determine the difference in the cycle performance between U-LNCM and Zr-LNCM electrodes, the differential capacity (dQ dV^{-1}) profiles were obtained by differentiating the 5th, 10th, 15th, and 30th charge/discharge curves (Fig. S3†). Both electrodes underwent the multiple phase transitions (H1→M→H2→H3) during the delithiation process. It is known that an abrupt anisotropic lattice contraction occurs in the c-axis direction during the final H2→H3 phase transition, which is responsible for particle cracking and consequent capacity fading.[49,50] For the U-LNCM electrode, the cell polarization (potential gap

between cathodic peak and anodic peak) increased and the intensity of H2➔H3 transition peak decreased with cycles, indicating the irreversible structural damage during multiple cycles. However, the position and intensity of H2➔H3 peak were relatively well maintained in the Zr-LNCM electrode; thus, the irreversibility was significantly reduced, which agrees well with the improved cycle stability. The enhanced cycle stability and increased reversibility of dQ dV^{-1} analysis further infers that Zr was incorporated into the layered oxide lattice. Furthermore, Zr doping improved the rate capability of LNCM, as shown in Fig. 2c. The discharge capacity of both electrodes steadily decreased with the stepwise increase of current density; however, the Zr-LNCM electrode delivered a higher discharge capacity at all the current densities, exhibiting the enhanced rate performance compared to the U-LNCM electrode. In particular, at the high current density of 2 C, the Zr-LNCM electrode delivered a high discharge capacity of 162.2 mAh g^{-1}, whereas the U-LNCM electrode only delivered a discharge capacity of 110.4 mAh g^{-1}. To determine the reason for the superior rate capability of Zr-LNCM electrode, the lithium-ion diffusion coefficient (D_{Li}^{+}) was measured using the galvanostatic intermittent titration technique (GITT) (Fig. S4†). The GITT measurement was performed by applying a current pulse of 0.2 C for 10 min to obtain the closed-circuit voltage (CCV) and subsequently resting for 1 h to obtain the quasi-open-circuit voltage (QOCV). Compared to the U-LNCM electrode, the Zr-LNCM electrode exhibited higher D_{Li}^{+} at all potentials (Fig. 2d). In particular, the sudden decrease of D_{Li}^{+} at ~4.15 V was significantly alleviated in the Zr-LNCM electrode; that is, ~90% of the lithium mobility decreased in U-LNCM, whereas only 54% decreased in the Zr-LNCM electrode. As the sudden decrease of D_{Li}^{+} at high potential was induced by the collapse of Li slab during the H2➔H3 phase transition,[28,35] the GITT results indicate that Zr doping alleviated the abrupt c-axis contraction during the phase transition, which positively contributed to the enhanced kinetics as well as cycle stability.

As the electrochemical stability of Ni-rich layered oxides is closely associated with the phase transitions during the charging process, *in-situ* XRD analysis was conducted to monitor the phase and structure evolution during delithiation (Fig. 3a). The electrodes were charged to 4.4 V (vs. Li/Li^{+}) at a current density of 0.2 C using the modified coin-type cell with 3 mm hole at its center sealed with mylar film. The electrodes were pre-cycled before the measurements, and the diffraction patterns were recorded every 10 min. During an early stage of delithiation, the (003)$_{H1}$ peak gradually shifted to lower 2θ for both electrodes. The shift of (003)$_{H1}$ peak to a lower 2θ indicates an enlargement of the c-axis, which is attributed to the increase of oxygen–oxygen repulsion due to a diminishing lithium-screening effect within the Li slab.[51] However, upon further delithiation, the (003)$_{H2}$ peak rapidly shifted toward higher 2θ, which implies the sudden lattice collapse along the c-axis direction. The U-LNCM electrode exhibited a peak shift of 1.06° at high SOC, whereas a smaller peak shift of 0.88° was observed for the Zr-LNCM electrode. Thus, the above results imply that Zr doping effectively alleviated the c-axis contraction at high SOC, suggesting that the incorporation of Zr into the crystal lattice noticeably

mitigated the intrinsic structural change associated with the multiple phase transitions during charging. [7,35] Furthermore, as the sudden lattice contraction localizes the stress within the secondary particle that could lead to the particle crack formation/propagation, it is expected that the Zr-LNCM electrode would be more resistant against the mechanical fracture.[52] Thus, to visualize the effect of Zr incorporation on the crack formation, the microstructures of pristine and cycled electrodes were investigated using the cross-sectional SEM. For both U-LNCM and Zr-LNCM pristine electrodes, no obvious crack or disintegration was observed and the primary particles were closely attached to each other (Fig. 3b). However, a manifest difference between U-LNCM and Zr-LNCM was observed after multiple cycling (Fig. 3c, S5†). For the cycled U-LNCM, primary particles were disintegrated from each other, and some of the cracks were propagated from the particle surface toward the inner bulk. These cracks provide a pathway for the electrolyte infiltration, and the direct exposure of in-grain primary particles to the electrolyte would provoke the unwanted parasitic reactions within the inner bulk and thus increase the cell impedance.[9,53] In contrast, no visible structural collapse was detected for the cycled Zr-LNCM, and only minor particle disintegration was observed, which is attributed to the alleviation of sudden c-axis contraction upon high SOC. These results indicate the superior effects of Zr doping in stabilizing the intrinsic and extrinsic structural collapse of LNCM that are associated with the sudden c-axis contraction during the multiple cycling.

As the Ni-rich layered oxides are deteriorated by multiple degradation mechanisms besides the structural collapse, further analyses were conducted employing STEM-EELS, DEMS, and STEM imaging to elucidate the origin of the enhanced cycle performance in the Zr-LNCM electrode. Considering the strong correlation between surface degradation and cathode deterioration, we first examined the electronic states of the cycled electrodes using electron energy loss spectroscopy (EELS). The change of the oxidation states was determined by probing the TM L-edge and O K-edge EELS spectra.[54] Specifically, the change of the peak position in the TM L spectrum and the absence/decrease of the pre-edge peak in the O K spectrum can be utilized to trace the change of the TM valence state and detect the oxygen loss from the particle, respectively.[55,56,57] Among the TM L-edges, only Ni L-edge was examined as Ni is more than 92% in this study and acts as a main culprit for the continuous capacity fading in Ni-rich layered cathodes. The EELS spectra were obtained by performing the line scan from the surface to the bulk in the 50th cycled U-LNCM and Zr-LNCM electrodes along the same crystallographic orientation. For both U-LNCM (Fig. 4a) and Zr-LNCM (Fig. 4b), the surface L$_3$ peaks of the Ni L-edge were positioned at lower energy compared with that of the bulk, indicating the reduction of the Ni valence state at the particle surface.[55] The L-edge peaks smoothly shifted toward higher energy when scanning from the surface to the bulk, and the bulk values were obtained at 8–9 nm and 4 nm from the surface for U-LNCM and Zr-LNCM, respectively. This result implies that U-LNCM had undergone more severe Ni reduction at the particle surface than Zr-LNCM. Likewise, the O pre-edge peak was absent at the surface, which was clearly different with the bulk peak. However,

the pre-edge peak gradually evolved and the intensity increased when moving from the surface to the bulk. The O pre-edge peak recovered its bulk peak at 8–9 and 4 nm from the surface for U-LNCM and Zr-LNCM, respectively. Thus, the intensity reduction of the O K pre-edge peak corresponded well to the shift of the L_3-edge peak position in both electrodes. Therefore, both EELS Ni L-edge and O K-edge spectra imply that Zr-LNCM was more resistant to the oxygen-vacancy formation during cycling than U-LNCM. After confirming the positive effect of Zr doping on the oxygen-vacancy formation, *operando* differential electrochemical mass spectrometry (DEMS) was conducted to compare the gas evolution rate during the charge process. The DEMS measurements were performed at a current density of 0.1 C with a high mass loading of ~10 mg cm^{-2}. For both cathodes, the O_2 gas was detected after the H2 phase, and the gas evolution increased upon further increasing the charge potential (Fig. 4c). The rapid increase of gas evolution upon increasing the charge potential is due to the unstable LNCM layered structure in the high delithiated state.[25] Furthermore, the CO_2 gas, which is produced by the electrolyte decomposition from the released singlet oxygen from LNCM,[12,17] was concurrently evolved with the O_2 gas, and the rate also increased with increasing the charge voltage (Fig. 4d). Meanwhile, the Zr doping delayed the onset time of gas evolution and reduced the rate of O_2 gas evolution compared to those for U-LNCM (Fig. 4c). In addition, the CO_2 gas evolution was mitigated, indicating that the chemical oxidization of the electrolyte was effectively suppressed by the Zr doping (Fig. 4d). Thus, the *operando* DEMS results further confirmed that Zr doping of LNCM alleviated the oxygen gas release as well as the electrolyte decomposition. Finally, the surface of the pristine and cycled LNCM electrodes were examined using atomic-resolution STEM to reveal the structure transformation resulting from the oxygen loss. The STEM images of the pristine electrodes revealed a very thin cation-mixed layer on the surface (Fig. S6†). After 50 cycles at 0.3 C, the bulk retained its original pristine R-3m layered structure for both electrodes (Fig. S7†); however, the SRL on the particle surface significantly propagated toward the inner bulk, which was indexed as the NiO-like rock salt (Fm-3m) phase using the fast Fourier transform (FFT) pattern (Fig. 4e, f). The thickness of the SRL was estimated to be ~8 and ~4 nm for U-LNCM and Zr-LNCM, respectively; thus, Zr doping also alleviated the detrimental cation mixing during cycling. The alleviation of cation-mixing behavior by the Zr doping is highly related to the suppression of oxygen vacancy formation,[58] which can be supported by our EELS and DEMS results.

Overall, by adopting various analysis techniques, we have uncovered that Zr doping enhanced the LNCM electrochemical performance by alleviating the diverse LNCM degradation factors, including abrupt c-axis contraction, microcrack formation, oxygen release, electrolyte decomposition, and Li–Ni cation mixing. These factors continuously degraded the LNCM during the multiple cycles and resulted in the impedance rise, as confirmed by the EIS measurements (Fig. S8†). The charge-transfer resistance (R_{ct}) of U-LNCM progressively increased from 334 Ω (5th cycle) to 2122 Ω (100th cycle at 0.3 C), whereas that of Zr-LNCM marginally increased from 258 Ω (5th cycle) to 723 Ω (100th cycle at 0.3 C). Therefore, the

EIS measurements further confirmed the positive effect of Zr doping on alleviating the degradation of the Ni-rich layered cathode.

4 Discussions

We have shown that Zr doping substantially enhanced the cycle and rate performance of LNCM, and by combining microscopy and spectroscopy techniques, we revealed that the Zr dopant alleviated most of well-known degradation factors of Ni-rich layered cathodes. Our discussion mainly focuses on determining the fundamental origin of the Zr doping mechanism in Ni-rich layered cathodes. The instability of lattice oxygen upon deep charge has been proposed as one of the critical origins of the general capacity decay in the layered oxides. The lattice oxygen instability is due to the oxygen charge depletion ($O^{2-} \rightarrow O^{-2+\delta}$) resulting from the O$\rightarrow$Ni charge transfer mechanism, which activates the Li–O collapse (lattice contraction along the c-axis) and oxygen gas evolution.[12,16,17,28] The sudden Li–O collapse localizes the stress within the secondary particle, which could develop into the microcrack formation.[45] The release of oxygen gas leaves an oxygen vacancy within the layered oxide, providing a Ni migration pathway that accelerates the cation mixing.[58] Furthermore, the released oxygen is in the highly reactive singlet oxygen gaseous state that reacts and chemically decomposes the electrolyte.[17] Therefore, as the instability of lattice oxygen triggers the various degradation mechanisms of Ni-rich layered oxides and can be considered as the critical degradation origin, the investigation of Zr doping on the oxygen stability is needed to fully understand the Zr doping on the layered cathodes.

To obtain insight into the oxygen charge transfer involved in the delithiation process, the magnetic moment of the charged samples was collected by Squid-VSM analysis. Note that Squid-VSM analysis detects the bulk magnetic moment of the sample.[59] The paramagnetic effective moment (μ_{eff}) of the charged sample can be extracted from the temperature dependence of the reciprocal magnetic susceptibility $\chi^{-1}(T)$.[60-63] Briefly, an increase of the slope in the curve of χ^{-1} vs. T indicates a decrease of the magnetic moment of the sample.[63-65] In Ni-rich LNCM, Ni acts as a main redox center with the oxidation state Ni^{3+} (electronic configuration: $t_{2g}^6 e_g^1$) for the pristine electrode, whereas it oxidizes to Ni^{4+} (electronic configuration: $t_{2g}^6 e_g^0$) during delithiation. Therefore, as the unpaired electron in the e_g band is removed from Ni during the delithiation process, it is expected that the magnetic moment of the sample would decrease upon charge, thereby increasing the slope in the χ^{-1} vs. T curve. The SOC positions at which the measurements were taken are shown in Fig. 5a. From the obtained χ^{-1} vs. T measurements, the samples followed the Curie–Weiss law $\chi = C/(T-\Theta)$, where C is the Curie constant and Θ is the Curie–Weiss temperature (Fig. 5b, c). Based on the previous reports, the temperature region of 100–250 K was fitted to the Curie–Weiss law to obtain the paramagnetic effective moment.[63,64] As expected, during the early stage of delithiation, the slope of $\chi^{-1}(T)$ curve increased with increasing SOC for both U-LNCM (Fig. 5b) and Zr-LNCM (Fig. 5c). However, when the SOC reached x=0.88 ($Li_{1-x}MO_2$,

x=0.88 corresponds to the capacity obtained when 4.4 V charged), a sudden decrease of the slope was observed for U-LNCM. The calculated paramagnetic effective moment (μ_{eff}) steeply increased over 40% at x=0.88 for U-LNCM (Fig. 5d). Several scenarios were considered (Supplementary Note 1), and it was determined that the increase of the magnetic moment can be explained by the oxygen charge transfer mechanism, which produces the abundant unpaired electrons within oxygen and nickel that could contribute to the dramatic increase of μ_{eff} (Fig. 5e).[60,63,66] In contrast, for Zr-LNCM, the increase of slope at x=0.88 was not dramatic compared to that of U-LNCM, showing only a 14% increase of μ_{eff} (Fig. 5c, d). The above results indicate that Zr doping effectively restrained the charge transfer between O and Ni.

The above Squid-VMS results are further evidenced by mapping of resonant inelastic X-ray scattering (mRIXS) (Fig. 6a, Fig. S9†), which has been demonstrated as a tool-of-choice to detect the oxidized oxygen in the bulk lattice of battery cathodes due to its ability to deconvolute the oxidized oxygen and TM-O hybridization signals.[67-71] In particular, the feature around 531.0 and 523.7 eV excitation and emission energy (marked by pink arrows), respectively, is a fingerprint of oxidized oxygen in the battery electrodes. Additionally, this fingerprint feature always shows up together with the enhanced intensity close to the elastic peak (marked by yellow arrows).[68-70] The mRIXS results showed that the oxidized oxygen feature was not observed until x=0.8 ($Li_{1-x}MO_2$) for both U-LNCM and Zr-LNCM (Fig. S9†), but emerged at x=0.88 for U-LNCM; in contrast, Zr-LNCM showed a negligible feature even at high SOC (Fig. 6a). Moreover, the low energy loss feature (marked by yellow arrows) close to the elastic peak of U-LNCM electrode displayed the enhanced intensity than the Zr-LNCM electrode at x=0.88. For a more direct comparison, super-partial fluorescence yield (sPFY) spectra, which are obtained by integrating the intensity within the emission energy window around 523.7 eV ± 1 eV of mRIXS data,[70,71] has been conducted at x=0.88. As shown in Fig. 6b, the fingerprinting peak of oxidized oxygen at 531 eV was clearly observed for U-LNCM whereas it was hardly observed in Zr-LNCM, further implying that more oxidized oxygen was present in U-LNCM compared to Zr-LNCM at high SOC. After confirming the difference in the oxidized oxygen between U-LNCM and Zr-LNCM, we investigated the change of the Ni valence state during delithiation. Fig. 6c shows the variation of the Ni L_3-edge absorbance spectra obtained using scanning transmission X-ray microscopy (STXM). When charged from x=0 ($Li_{1-x}MO_2$) to x=0.8, the intensity of the peak at ~855 eV increased for both U-LNCM and Zr-LNCM, indicating an increase of the Ni valence state.[72] However, upon deep charge at x=0.88, the intensity of the peak at 855 eV significantly decreased compared to that at x=0.8 in U-LNCM, whereas a minimal peak change was observed for Zr-LNCM. These results indicate that Ni in U-LNCM underwent a severe valence reduction at x=0.88, where the oxidized oxygen was present. Overall, by combining mRIXS and STXM analyses, it is evident that the O→Ni charge transfer is involved in U-LNCM upon delithiation and that Zr doping effectively mitigated this phenomenon.

To gain a fundamental understanding of Zr doping effect on the oxygen charge evolution of LNCM cathodes, we performed the first-principles calculations using the projector augmented wave (PAW) method. The $Li_{1-x}NiO_2$ model system was used for the density functional theory (DFT) calculations as the Ni content was over 90% in this study. Zr was positioned on the Ni site according to the previous reports.[38,48] The evolution of oxygen charge density was evaluated by varying the lithium content in the $Li_{1-x}NiO_2$ system and the oxygen charge density was compared between oxygen atoms near Zr atom and those far from Zr atom. The number around the oxygen atoms in Fig. 6e and 6f indicates the oxygen charge loss upon delithiation. On deep charging (x=0.84), O atoms are under a charge deficiency state compared to that at x=0 (pristine state) (Fig. 6e, 6f), which matches well with the previous reports.[28,73] However, the calculation results showed that O atoms near Zr atom (Fig. 6f) lost
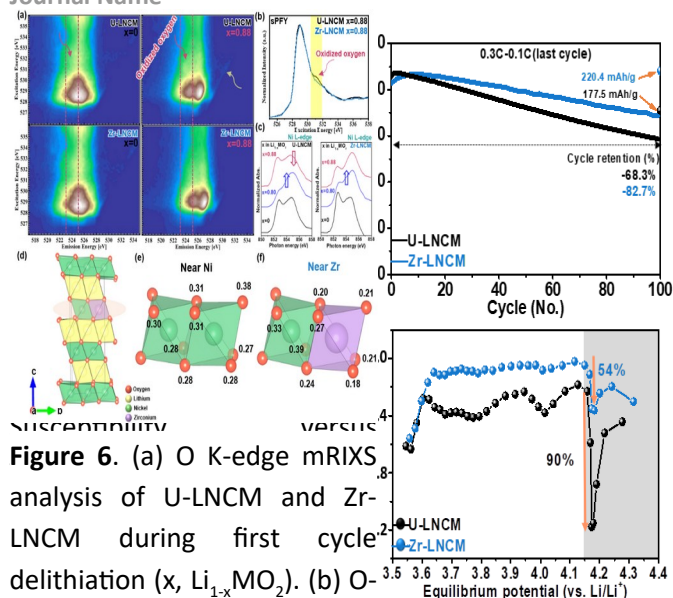
Figure 6. (a) O K-edge mRIXS analysis of U-LNCM and Zr-LNCM during first cycle delithiation (x, $Li_{1-x}MO_2$). (b) O-K mRIXS-sPFY analysis of U-LNCM and Zr-LNCM at x=0.88 state, where the peak on the shaded area around 530~532 eV indicates the oxidized oxygen. (c) Ni L-edge STXM results of U-LNCM and Zr-LNCM during first cycle delithiation (x, $Li_{1-x}MO_2$). (d) Atomic structure of $Li_{12}Ni_{11}ZrO_{24}$, (e) atomic structure near Ni atom, and (f) atomic structure near Zr atom. The number on (e) and (f) indicates the charge loss of corresponding oxygen when delithiated from $Li_{12}Ni_{11}ZrO_{24}$ to $Li_2Ni_{11}ZrO_{24}$, which is obtained by the Bader charge analysis.

less charge density compared to those of O atoms far from Zr atom (Fig. 6e). Therefore, the DFT calculations were consistent with the experimental results, showing that Zr doping was effective in restraining the oxygen charge loss upon deep charge.

Previous first-principles calculations revealed that high-valent dopants (W, Ta, Ti, etc.) can stabilize the lattice oxygen owing to the strong electron hybridization effect with the oxygen in the layered oxide system.[74,75] In addition, experimental studies have shown that these dopants enhanced the Ni-rich layered cathode cyclability by alleviating the lattice contraction, crack propagation, oxygen evolution, and surface reconstruction.[2-5] In particular, the stabilization of lattice oxygen by Ti doping has been previously

evidenced by mRIXS and DFT calculation, with similar results as those for Zr doping.[73] Based on these results, the effect of Zr doping on the oxygen stability can be rationalized as strong Zr–O hybridization through high-valent Zr^{4+}, which can confirmed from our crystal orbital Hamilton population (COHP) results in Table S4 and Supplementary Note 2.

Thus far, we have unveiled that the oxygen charge-transfer mechanism was involved in the high SOC state of LNCM and that Zr doping successfully mitigated this phenomenon. When the charge is transferred from O→Ni, a hole resides on the oxygen that leads to the instability of lattice oxygen. Furthermore, the instability of lattice oxygen can provoke lattice collapse and oxygen evolution, which can additionally cause particle cracking and electrolyte decomposition, eventually leading to the capacity fading. However, as the Zr doping effectively mitigates the oxygen charge transfer, the oxidation of oxygen at high SOC could be relatively suppressed compared to the undoped cathode, thus possibly alleviating the following-up degradation mechanisms. To prove this, the temperature-resolved heating XRD analysis was performed for both 4.4 V charged U-LNCM and Zr-LNCM electrodes. For U-LNCM, the sample was fully decomposed at 480 °C while the decomposition temperature was delayed to 520 °C in Zr-LNCM (Fig. S10†). As the thermal decomposition of the charged cathode is induced by the instability of the lattice oxygen framework,[13,76] the delay of decomposition through Zr doping indicates a relatively stabilized lattice structure by the relaxation of oxygen charge transfer. Therefore, by combining the obtained results in this study, we propose "lattice oxygen stabilization" as the potential origin of the Zr doping mechanism.

5 Conclusions

Herein, an in-depth study was conducted to unveil the Zr doping mechanism in Ni-rich layered cathodes for LIBs. First, by combining various spectroscopic techniques, we showed that Zr doping enhanced the Ni-rich LNCM electrochemical performance by alleviating most of the well-known LNCM degradation factors starting from the surface to the bulk. Then, to determine the true origin of the doping mechanism, Squid-VSM along with state-of-the-art mRIXS were selected as the tools of choice to clarify the role of Zr doping. From the analysis, we uncovered that the oxygen charge-transfer mechanism was involved in the LNCM deep charge state, causing sudden lattice contraction as well as other degradation factors. However, when Zr was incorporated into the LNCM crystal structure, the oxygen charge transfer was effectively mitigated, thus aiding in suppressing the subsequent degradation mechanisms to enhance the cathode cycle life. Therefore, the obtained results suggest the importance of examining the relationship between dopant and lattice oxygen stability to unveil its mechanism. This work enhances our understanding of the doping effects in Ni-rich layered oxides and provides insight for further improvements in state-of-the-art Li ion battery cathode materials.

ARTICLE

Conflicts of interest

There are no conflicts to declare.

Acknowledgements

Notes and references

1   J. Wang, Y. Yamada, K. Sodeyama, C. H. Chiang, Y. Tateyama, A. Yamada, *Nat. Commun*. 2016, **7**, 12032.

2   G. -L. Xu, X. Liu, A. Daali, R. Amine, Z. Chen, K Amine, *Adv. Funct. Mater*. 2020, **30**, 2004748.

3   W. Li, E. M. Erickson, A. Manthiram, *Nat. Energy.* 2020, **5**, 26-34.

4   C. -H. Jung, D. –H. Kim, D. Eum, K.- H. Kim, J. Choi, J. Lee, H. –H. Kim, K. Kang, S. –H. Hong, *Adv. Funct. Mater*. 2021, **31**, 2010095.

5   Y. Xia, J. Zheng, C. Wang, M. Gu, *Nano Energy*. 2018, **49**, 434-452.

6   U. -H. Kim, G. -T. Park, B. -K. Son, G. W. Nam, J. Liu, L. -Y. Kuo, P. Kaghazchi, C. S. Yoon, Y. -K. Sun, *Nat. Energy.* 2020, **5**, 860-869.

7   H. -H. Ryu, K. -J. Park, C. S. Yoon, Y. -K. Sun, *Chem. Mater*. 2018, **30**, 1155-1163.

8   Q. Xie, W. Li, A. Manthiram, *Chem. Mater*. 2019, **31**, 938-946.

9   U. H. Kim, D. W. Jun, K. J. Park, Q. Zhang, P. Kaghazchi, D. Aurbach, D. T. Major, G. Goobes, M. Dixit, N. Leifer, C. M. Wang, P. Yan, D. Ahn, K. H. Kim, C. S. Yoon, Y. K. Sun, *Energy Environ. Sci*. 2018, **11**, 1271-1279.

10 S.-K. Jung, H. Gwon, J. Hong, K.-Y. Park, D.-H. Seo, H. Kim, J. Hyun, W. Yang, K. Kang, *Adv. Energy Mater*. 2014, **4**, 1300787.

11 N. Li, S. Sallis, J. K. Papp, J. Wei, B. D. McCloskey, W. Yang, W. Tong, *ACS Energy Lett*. 2019, **12**, 2836-2842.

12 R. Jung, M. Metzger, F. maglia, C. Stinner, H. A. Gasteiger, *J. Phys. Chem. Lett*. 2017, **8**, 4820-4825.

13 S. Sharifi-Asl, J. Lu, K. Amine, R. Shahbazian-Yassar, *Adv. Energy Mater*. 2019, **9**, 1900551.

14 L. Mu, R. Lin, Rong Xu, L. Han, S. Xia, D. Sokaras, J. D. Steiner, T. -C. Weng, D. Nordlund, M. M. Doeff, Y. Liu, K. Zhao, H. L. Xin, F. Lin, *Nano Lett*. 2018, **18**, 3241-3249.

15 S. Lee, W. Jin, S. H. Kim, S. H. Joo, G. Nam, P. Oh, Y. -K. Kim, S. K. Kwak, J. Cho, *Angew. Chem. Int. Ed*. 2019, **58**, 2-10.

16 W. Li, H. Y. Asl, Q. Xie, A. Manthiram, *J. Am. Chem. Soc*. 2019, **141**, 5097-5101

17 J. Wandt, A. T. S. Freiber, A. Ogrodnik, H. A. Gasteiger, *Mater. Today.* 2018, **21**, 825-833.

18 M. D. Radin, S. Hy, M. Sina, C. Fang, H. Liu, J. Vinckeviciute, M. Zhang, M. S. Whittingham, Y. S. Meng, A. Van der Ven, *Adv. Energy Mater*. 2017, **7**, 1602888.

19 D. -H. Seo, J. Lee, A. Urban, R. Malik, S. Kang, G. Ceder, *Nat. Chem*. 2016, **8**, 692-697.

20 C. F. Petersburg, Z. Li, N. A. Chernova, M. S. Whittingham, F. M. Alamgir, *J. Mater. Chem. A*. 2012, **22**, 19993-20000.

21 M. Yoon, Y. Dong, Y. Yoo, S. Myeong, J. Hwang, J. Kim, S. -H. Choi, J. Sung, S. J. Kang, J. Li, Jaephil Cho, *Adv. Funct. Mater*. 2019, **30**, 1907903.

22 S. Sharifi-Asl, F. A. Soto, T. Foroozan, M. Asadi, Y. Yuan, R. Deivanayagam, R. Rojaee, B. Song, X. Bi, K. Amine, J. Lu, A. Salehi-khojin, P. B. Balbuena, R. Shahbazian-Yassar, *Adv. Funct. Mater*. 2019, **29**, 1901110.

23 K. Luo, M. R. Roberts, R. Hao, N. Guerrini, D. M. Pickup, Y. -S. Liu, K. Edstrom, J. Guo, A. V. Chadwick, L. C. Duda, P. G. Bruce, *Nat. Chem*. 2016, **8**, 684-691.

24 Q. Xie, W. Li, A. Dolocan, A. Manthiram, *Chem. Mater*. 2019, **31**, 8886-8897.

25 R. Jung, M. Metzger, F. Maglia, C. Stinner, H. A. Gasteiger, *J. Electrochem. Soc*. 2017, **164**, A1361-A1377.

26 C. Sun, X. Liao, F. Xia, Y. Zhao, L. Zhang, S. Mu, S. Shi, Y. Li, H. Peng, G. V. Tendeloo, K. Zhao, J. Wu, *ACS Nano*. 2020, **14**, 6181-6190.

27 Z. Zhu, D. Yu, Z. Shi, R. Gao, X. Xiao, I. Waluyo, M. Ge, Y. Dong, W. Xue, G. Xu, W. -K. Lee, A. Hunt, J. Li, *Energy Environ. Sci*. 2020, **13**, 1865-1878.

28 A. O. Kondrakov, H. Geßwein, K. Galdina, L. d. Biasi, V. Meded, E. O. Filatova, G. Schumacher, W. Wenzel, P. Hartmann, T. Brezesinski, J. Janek, *J. Phys. Chem. C*. 2017, **121**, 24381-24388.

29 P. Yan, J. Zheng, T. Chen, L. Luo, Y. Jiang, K. Wang, M. Sui, J. -G. Zhang, S. Zhang, C. Wang, *Nat. Commun*. 2018, **9**, 2437..

30 K. Zhou, Q. Xie, B. Li, A. Manthiram, *Energy Storage Mater*. 2021, **34**, 229-240.

31 W. Liu, X. F. Li, D. B. Xiong, Y. C. Hao, J. W. Lia, H. R. Kou, B. Yan, D. J. Lia, S. G. Lu, A. Koo, K. Adair, X. L. Sun, *Nano Energy*. 2018, **44**, 111-120.

32 X. Xu, H. Huo, J. Jian, L. Wang, H. Zhu, S. Xu, X. He, G. Yin, C. Du, X. Sun, *Adv. Energy Mater*. 2019, **9**, 1803963.

33 U. H. Kim, H. H. Ryu, J. H. Kim, R. B. Mücke, P. Y. Kaghazchi, C. S. Yoon, and Y. K. Sun, *Adv. Energy Mater*. 2019, **9**, 1803902.

34 T. Weigel, F. Schipper, E. M. Erickson, F. A. Susai, B. Markovsky, D. Aurbach, *ACS Energy Lett*. 2019, **4**, 508-516.

35 H. -H. Ryu, G. -T. Park, C. S. Yoon, Y. -K. Sun, *J. Mater. Chem. A*. 2019, **7**, 18580-18588.

36 Q. Li, Z. Li, S. Wu, Z. Wang, X. Liu, W. Li, N. Li, J. Wang, W. Zhuang, *ACS Appl. Energy Mater*. 2020, **3**, 11741-11751.

37 J. H. Choi, S. Y. Lee, S. M. Yoon, K. H. Kim, M. Kim, S. H. Hong, *ChemSusChem*. 2019, **12**, 2439-2446.

38 F. Schipper, M. Dixit, D. Kovacheva, M. Talianker, O. Haik, J. Grinblat, E. M. Erickson, C. Ghanty, D. T. Major, B. Markovsky, D. Aurbach, *J. Mater. Chem. A*. 2016, **4**, 16073-16084.

39 F. Schipper, H. Bouzaglo, M. Dixit, E. M. Erickson, T. Weigel, M. Talianker, J. Grinblat, L. Burstein, M. Schmidt, J. Lampert, C. Erk, B. Markovsky, D. T. Major, D. Aurbach, *Adv. Energy Mater*. 2018, **8**, 1701682.

40 C. S. Yoon, U. -H. Kim, G. -T. Park, S. J. Kim, K. -H. Kim, J. Kim, Y. -K. Sun, *ACS Energy Lett*. 2018, **3**, 1634-1639.

41 J. Hong, H. -D. Lim, M. Lee, S. -W. Kim, H. Kim, S. -T. Oh, G. -C. Chung, K. Kang, *Chem. Mater.* 2012, **24**, 2692-2697.

42 G. Kresse, J. Furthmuller, *Phys. Rev. B*. 1996, **54**, 11169.

43 G. Kresse, D. Joubert, *Phys. Rev. B*. 1999, **59**, 1758.

44 V. I. Anisimov, J. Zaanen, O. K. Andersen, *Phys. Rev. B*. 1991, **44**, 943.

45 L. Wang, T. Maxisch, G. Ceder, *Phys. Rev. B*. 2006, **73**, 195107.

46 S. P. Ong, W. D. Richards, A. Jain, G. Hautier, M. Kocher, S. Cholia, D. Gunter, V. L. Chevrier, K. A. Persson, G. Ceder, *Comput. Mater. Sci*. 2013, **68**, 314-319.

47 W. Tang, E. Sanville, G. Henkelman, J. Phys.: Condens. Matter. 2009, 21, 084204.

48 Y. Kim, *Phys. Chem. Chem. Phys*. 2019, **21**, 12505-12517.

49 J. -H. Kim, H. -H. Ryu, S. J. Kim, C. S. Yoon, Y. -K. Sun, *ACS Appl. Mater. Interfaces*. 2019, **11,** 30936-30942.

50 A. Manthiram, B. Song, W. Li, *Energy Storage Mater*. 2017, **6**, 125-139.

51 H. Li, P. Zhou, F. Liu, H. Li, F. Cheng, J. Chen, *Chem. Sci*. 2019, **10**, 1374-1379.

52 H. -H. Ryu, N. -Y. Park, J. H. Seo, Y. -S. Yu, M. Sharma, R. Mucke, P. Kaghazchi, C. S. Yoon, Y. -K. Sun, *Mater. Today*. 2020, **36**, 73-82.

53 S. Xia, L. Mu, Z. Xu, J. Wang, C. Wei, L. Liu, P. Pianetta, K. Zhao, X. Yu, F. Lin, Y. Liu, *Nano Energy*. 2018, **53**, 753-762.

54 P. Yan, J. Zheng, Z. -K. Tang, A. Devaraj, G. Chen, K. Amin, J. -G. Zhang, L. -M. Liu, C. Wang, Nat. Nanotech. 2019, **14**, 602-608.

55 K. Jarvis, C. -C. Wang, M. Varela, R. R. Unocic, A. Manthiram, P. J. Ferreira, *Chem. Mater*. 2017, **29**, 7668-7674.

56 S. Sharifi-As, F. A. Soto, A. Nie, Y. Yuan, H. Asayesh-Ardakani, T. Foroozan, V. Yurkiv, B. Song, F. Mashayek, R. F. Klie, K. Amine, J. Lu, P. B. Balbuena, R. Shahbazian-Yassar, *Nano Lett*. 2017, **17**, 2165-2171.

57 D. Qian, B. Xu, M. Chi, Y. S. Meng, *Phys. Chem. Chem. Phys*. 2014, **16**, 14665-14668.

58 F. Kong, C. Liang, L. Wang, Y. Zheng, S. Perananthan, R. C. Longo, J. P. Ferraris, M. Kim, K. Cho, *Adv. Energy Mater*. 2019, **9**, 1802586.

59 Y. R. Song, F. Yang, M. -Y. Yao, F. Zhu, L. Miao, J. -P. Xu, M. -X. Wang, H. Li, X. Yao, F. Ji, S. Qiao, Z. Sun, G. B. Zhang, B. Gao, C. Liu, D. Qian, C. L. Gao, J. -F. Jia, *Appl. Phys. Lett*. 2012, **100**, 242403.

60 G. Klinser, M. Stuckler, H. Kren, S. Koller, W. Goessler, H. Krenn, R. Wurschum, *J. Power Sources.* 2018, **396**, 791-795.

61 J. Sugiyama, Y. Ikedo, K. Mukai, H. Nozaki, M. Månsson, O. Ofer, M. Harada, K. Kamazawa, Y. Miyake, J. H. Brewer, E. J. Ansaldo, K. H. Chow, I. Watanabe, T. Ohzuku, *Phys. Rev. B*. 2010, **82**, 224412.

62 S. Topolovec, H. Kren, G. Klinser, S. Koller, H. Krenn, R. Wurschum, *J Solid State Electrochem*. 2016, **20**, 1491-1496.

63 M. Freire, N. V. Kosova, C. Jordy, D. Chateigner, O. l. Lebedev, A. Maignan, V. Pralong, *Nat. Mater*. 2016, **15**, 173-177.

64 N. A. Chernova, M. Ma, J. Xiao, M. S. Whittingham, J. Breger, C. P. Grey, *Chem. Mater*. 2007, **19**, 4682-4693.

65 M. Labrini, F. Scheiba, A. Almaggoussi, M. Larzek, M. H. Braga, H. Ehrenberg, I. Saadoune, *Solid State Ionics*. 2016, **289**, 207-213.

66 C. F. Petersburg, Z. Li, N. A. Chernova, M. S. Whittingham, F. M. Alamgir, *J. Mater. Chem*. 2012, **22**, 19993-20000.

67 W. Yang, T. P. Devereaux, *J. Power Sources.* 2018, **389**, 188-197.

68 G. -H. Lee, J. Wu, D. Kim, K. Cho, M. Cho, W. Yang, Y. -M. Kang, *Angew. Chem. Int. Ed.* 2020, **59**, 8681-8688.

69 N. Li, S. Sallis, J. K. Papp, J. Wei, B. D. McCloskey, W. Yang, W. Tong, *ACS Energy Lett.* 2019, **4**, 2836-2842.

70 J. Wu, Z. Zhuo, X. Rong, K. Dai, Z. Lebens-Higgins, S. Sallis, F. Pan, L. F. J. Piper, G. Liu, Y. -d. Chuang, Z. Hussain, Q. Li, R. Zeng, Z. -X. Shen, W. Yang, *Sci. Adv*. 2020, **6**, eaaw3871.

71 K. Dai, J. Wu, Z. Zhuo, Q. Li, S. Sallis, J. Mao, G. Ai, C. Sun, Z. Li, W. E. Gent, W. C. Chueh, Y. -D. Chuang, R. Zeng, Z. -X. Shen, F. Pan, S. Yan, L. F. J. Piper, Z. Hussain, G. Liu, W. Yang, *Joule*. 2019, **3**, 518-541.

72 D. Eum, B, Kim, S, J, Kim, H, Park, J, Wu , S.-P. Cho, G. Yoon, M. H. Lee, S. -K. Jung , W. Yang , W. M. Seong, K. Ku, O. Tamwattana, S. K. Park, I. Hwang, K. Kang , *Nat. Mater*. 2020, **19**, 419-427.

73 J. -N. Zhang, Q. Li, C. Ouyang, X. Yu, M. Ge, X. Huang, E. Hu, C. Ma, S. Li, R. Xiao, W. Yang, Y. Chu, Y. Liu, H. Yu, X. -Q. Yang, X. Huang, L. Chen, H. Li, *Nat. Energy*. 2019, **4**, 594-603.

74 J. Cheng, L. Mu, C. Wang, Z. Yang, H. L. Xin, F. Lin, K. A. Persson, J. Mater. Chem. 2020, **8**, 23293-23303.

75 H. Yang, H. -H. Wu, M. Ge, L. Li, Y. Yuan, Q. Yao, J. Chen, L. Xia, J. Zheng, Z. Chen, J. Duan, K. Kisslinger, X. C. Zeng, W. -K. Lee, Q. Zhang, J. Lu, *Adv. Funct. Mater*. 2019, **29**, 1808825.

76 K. -W. Nam, S.-M. Bak, E. Hu, X. Yu, Y. Zhou, X. Wang, L. Wu, Y. Zhu, K.-Y. Chung, X.-Q. Yang, *Adv. Funct. Mater*. 2013, **23**, 1047-1063.